May 2016

Classification of Riparian Saltcedar in the Desert Southwest Using Landsat Data and the HANTS Algorithm

WRRI Miscellaneous Report No. 32

Dennis C. McCarville
Max P. Bleiweiss
Salim Bawazir
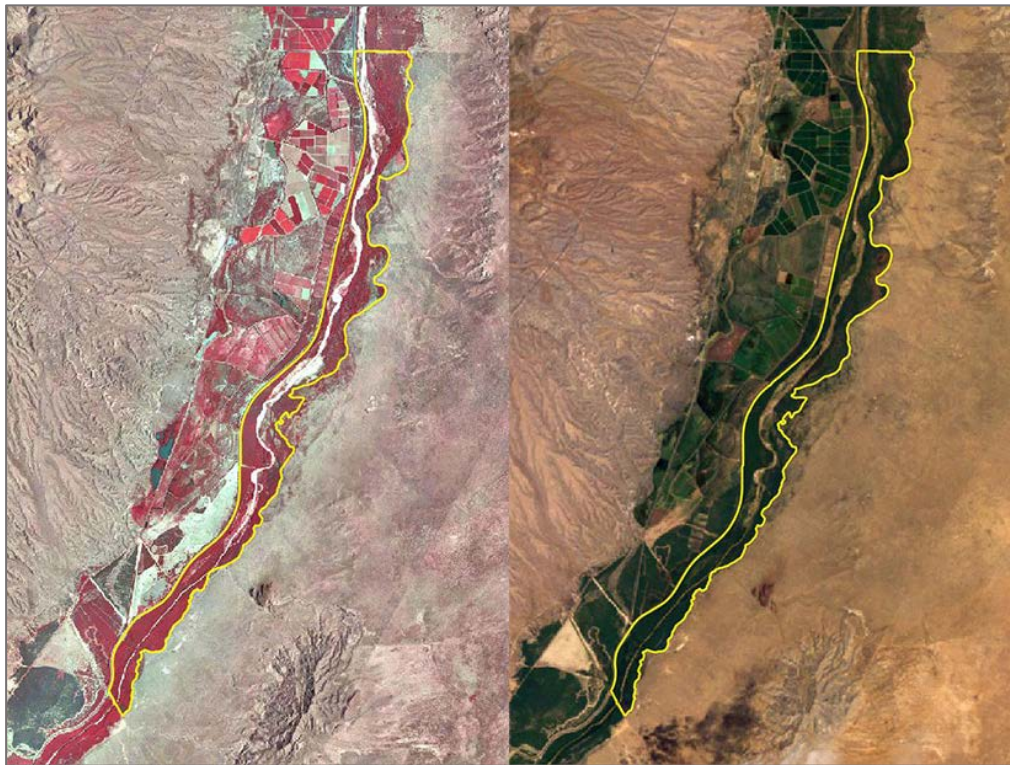
Near-Infrared (NIR) reflected light, which is the red color in the false-color NIR image, and the red reflected light in the natural RGB image can be used to calculate the Normalized Difference Vegetation Index (NDVI). NDVI values are used to indicate where and how much green biomass is in the observed area. The HANTS algorithm was used to process multiple NDVI images, and the results of the process were classified to locate areas with concentrations of saltcedar.

CLASSIFICATION OF RIPARIAN SALTCEDAR IN THE DESERT SOUTHWEST USING LANDSAT DATA AND THE HANTS ALGORITHM

By

Dennis C. McCarville
Elephant Butte Irrigation District

Max P. Bleiweiss
Entomology Plant Path and Weed Science
New Mexico State University

Salim Bawazir
Civil and Geological Engineering
New Mexico State University
and
ReNUWIt Engineering Research Center
Stanford University

Miscellaneous Report No. M32

May 2016

DISCLAIMER

The purpose of the Water Resources Research Institute technical reports is to provide a timely outlet for research results obtained on projects supported in whole or in part by the Institute. Through these reports, we are promoting the free exchange of information and ideas, and hope to stimulate thoughtful discussions and actions that may lead to resolution of water problems. The WRRI, through peer review of draft reports, attempts to substantiate the accuracy of information contained in its reports, but the views expressed are those of the authors and do not necessarily reflect those of the WRRI or its reviewers. Contents of this publication do not necessarily reflect the views and policies of the Department of the Interior, nor does the mention of trade names or commercial products constitute their endorsement by the United States government.

ACKNOWLEDGMENT

ABSTRACT

Saltcedar (*Tamarix* spp.) is one of the most invasive species threatening the ecosystem health in riparian regions across the southwestern United States. This research compared maps of saltcedar growth in the Bosque del Apache National Wildlife Refuge derived using traditional pixel-wise classification methods, to maps derived from a series of normalized difference vegetation index (NDVI) images that were processed using the harmonic analysis of time series (HANTS) algorithm. For 2000/2001 the overall prediction accuracies for saltcedar classification based on traditional methods ranged from 88.0 to 91.0%. Corresponding overall accuracies based on the HANTS algorithm ranged from 81.5 to 90.5%. For 2010/2011 the overall prediction accuracies for saltcedar classification based on traditional methods ranged from 88.0 to 89.0%. Corresponding overall accuracies based on the HANTS algorithm ranged from 77.5 to 85.0%. The traditional classification required more data preparation and expertise than the HANTS based classification; however, the HANTS based classification required a larger dataset. The results show that the HANTS reconstruction of NDVI data can be used directly to classify areas with saltcedar. The phenological changes revealed by the HANTS algorithm reconstruction could also be used to select data used with other classification methods.

Keywords: HANTS algorithm; NDVI; saltcedar; remote sensing; Landsat

TABLE OF CONTENTS

1   Introduction

Controlling the spread of invasive saltcedar (*Tamarisk* spp.) in riparian areas has long been recognized as a challenge by land managers. Since its introduction to the United States in the early 1800s and its subsequent spread across the southwestern United States, there have been numerous studies have investigated saltcedar in riparian areas[1]. Determining the areal extent of saltcedar using hyperspectral remote sensing imagery[2-6] and moderate resolution remote sensing imagery[7-10] has been investigated.

The problem with using hyperspectral data to map saltcedar is that imagery is expensive to acquire and often not available for the required period or location. Landsat moderate resolution satellite imagery can be downloaded from the Internet at no charge and includes data archives extending back in time to the mid-1970s. Although moderate resolution imagery does not supply the detailed information that hyperspectral imagery can produce, it does provide information that can support land-management planning. Many previous studies have investigated the use of Landsat data for identifying landcover; however, it has been demonstrated that some traditional remote sensing classification methods may not provide the same level of accuracy in every region (or even different time periods in the same region), even when the environmental conditions initially appear to be very similar.[11] For this reason, the continued investigation of alternative methods of identifying saltcedar using remote sensing data is needed.

This study demonstrates the value of using multiple methods for mapping saltcedar, as each method provides useful information on riparian saltcedar. Two methods were investigated: the first method used stacked layers of spectral profiles and products derived from selected

1

Landsat imagery (e.g., Tasseled Cap[12] and land-surface temperature), and the second method

used a series of normalized difference vegetation index (NDVI) images derived from Landsat

data together with the harmonic analysis of time series (HANTS) algorithm. The HANTS

algorithm uses the Fast Fourier Transform (FFT) algorithm that has been used with NDVI to

map agroecological zones in vegetation growth,[13] investigate periodic climate processes[14] and

land-surface phenologies,[15] to characterize seasonal changes for natural and agricultural land

use/time,[16] and investigate the impacts of rainfall anomalies.[17] Although the HANTS algorithm

was originally devised to remove cloud contamination and reconstruct gapless imagery at

prescribed times using temporal interpolation,[18] it has also been used to investigate the

phenological response of vegetation to variations in river flow.[19]

The HANTS algorithm removes cloud contamination by calculating a Fourier series to model a

time series of pixelwise observations. The time signal for each pixel is modeled using

harmonic sine and cosine waves fitted to the period of a complete cycle implied by the

imagery. In the case of remote sensing imagery, typical cycles include annual (e.g., the

seasonal growth of vegetation) and diurnal cycles (e.g., the hourly variation in local solar

elevation). During the HANTS fitting process, outliers are identified and replaced with the

values given by the Fourier series. HANTS outputs a smoothed time series of imagery where

the high frequency information such as that caused by cloud cover has been removed. In

addition, the imagery does not have to be evenly spaced in time when using the HANTS

algorithm. In this study, the HANTS algorithm was applied to a series of NDVI images derived

from the Landsat-5 Thematic Mapper (TM) data. The hypothesis was that the HANTS output,

when combined with an appropriate classification technique, based, for example, on the slope

of the smoothed time series, would reveal the phenological changes of the riparian vegetation[20,]

[21] , thus allowing areas with saltcedar to be differentiated from other vegetation types. Since the HANTS algorithm preserves most of the phenological information embedded in the data, forehand knowledge of the study area's plant phenology may be unnecessary, if the phenology signal is sufficiently strong.

2 Methods

2.1 Description of the Study Area

The study area (Fig. 1) encompasses the riparian region of Bosque del Apache National Wildlife Refuge (NWR) located in central New Mexico, U.S.A. The total area of the Bosque del Apache NWR is about 23,162 ha of which 3,440 ha are in the floodplain[22]. The riparian portion of Bosque del Apache NWR studied is approximately 1,600 ha. To the northwest are the Chupadera Mountains and to the southeast are the Little San Pascual Mountains. The Rio Grande runs through the Refuge and is bordered by riparian vegetation. The terrain ranges from flat lands by the river floodplain to the mountainous land. The elevation of the flood plain averages 1370 m above sea level (North American Datum of 1927, NAD 27).

The area's climate is typical of the semiarid region of the southwestern United States. Bawazir,[23] using climate data of the area from 1948 through 1992, reported mean annual total precipitation of 223 mm, mean maximum temperature for June, July and August of 34.62 °C, 35.11 °C and 33.63 °C, respectively, and mean minimum temperature of -6.34 °C and -6.37 °C for January and December.

The vegetation at the Bosque del Apache NWR is well described by Taylor and McDaniel.[22] The riparian vegetation primarily included mixed saltcedar/bosque and homogenous thickets of saltcedar (*Tamarix* spp.) and cottonwood (*Populus fremontii*). The vegetation species include

black willow (*Salix nigra*), coyote willow (*Saliz exigua*), seepwillow (*Baccharis glutinosa*), false indigo (*Amorpha fruticosa*), screwbean mesquite (*Prosopis pubescens*), wolfberry (*Lycium andersonii*), fourwing saltbush (*Atriplex canescens*), Russian olive (*Elaeagnus angustifolia*), and other sporadic understory weeds.
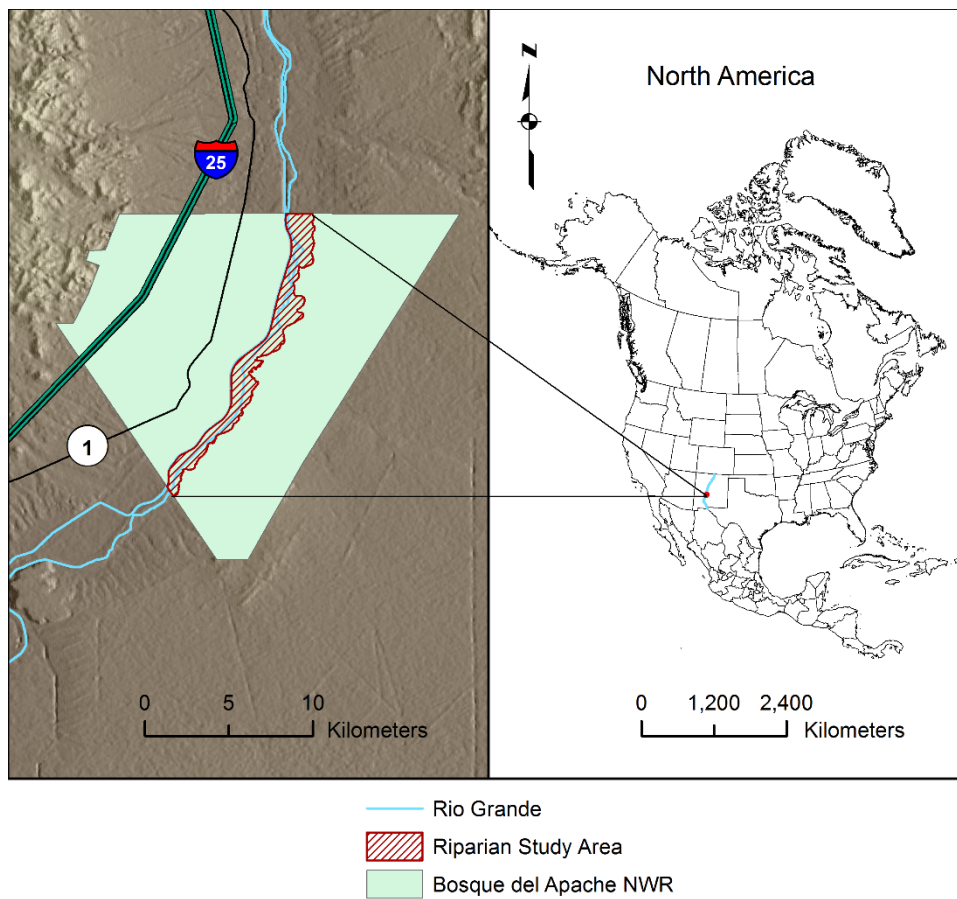
Fig. 1 Bosque del Apache National Wildlife Refuge (NWR) and riparian study area.

2.2 Datasets

The Bosque del Apache NWR is located in a region that is overlapped by two Landsat paths, so that Landsat-5 TM satellite data from Path 34 Row 36 and Path 33 Row 37 were used. Since the east and west edges of Landsat-7 data (where the Bosque del Apache NWR is located) were most affected by the failure of the scan line corrector in 2003, Landsat-7 imagery was not used for this study. There were 30 cloud-free Landsat-5 TM images ranging from November 1999 to April 2001 for the first period, and 42 cloud-free images ranging from November 2009 to May 2011 for the second period of the HANTS based trials.

A smaller series of four cloud-free Landsat images from December 2000 to August 2001 and from December 2010 to August 2011 were used for the multi-spectral trials (Table 1). The images were selected to reflect the declining, minimum, rising, and maximum phases of the annual NDVI cycle (See Table 1), which relate to the overall green vegetation phenological cycle. The minimum NDVI values generally coincide with the dormant phase, and the declining and rising NDVI values correspond to senescence in the fall and greening of the vegetation in the spring. The maximum NDVI values indicate when the riparian area vegetation has maximum green leaf coverage. The phases were identified using the maximum study area NDVI values from the NDVI series derived from the HANTS based trials. The dates were specifically selected to use the last data available before the termination of the Landsat-5 program in 2011. The HANTS data for a preliminary study originally covered the same time frame; however, it was later decided that an entire growing season starting with the lowest NDVI values in early spring would be beneficial. Therefore the Landsat data for the HANTS algorithm based trials was extended backwards in time approximately one year.

Table 1 Dates of the selected Landsat data subsets as related to the NDVI cycle.

Series	Declining	Minimum	Rising	Maximum
2000 - 2001	12/18/2000	02/04/2001	03/24/2001	08/24/2001
2010 - 2011	12/14/2010	02/16/2011	03/29/2011	08/27/2011

U.S. Bureau of Reclamation (BOR) land-cover classification maps for 2002 and 2008 and digital ortho quarter quadrangles (DOQQ) aerial imagery with one-meter spatial resolution for years 1996, 2005, and 2011 were used to help select training and assessment points. A Garmin® GPSMAP® 60Cx handheld global positioning system (GPS) unit was used to collect coordinate data on saltcedar, cottonwood, and willow stands in June 2012.

The North American Regional Reanalysis[24] (NARR) dataset was used with the North American Atmospheric Correction Calculator[25] (NAMCORR) atmospheric correction parameter calculator to reduce distortion of Landsat thermal band imagery caused by the atmosphere. The NARR data cover North America with a 32-kilometer spatial resolution and a three-hour temporal resolution.[26]

2.3 Classification – Selected Imagery

Two methods were investigated for classifying areas with saltcedar in 2010 - 2011, which were then repeated for the period 2000 - 2001. The first method was based on stacking the reflective Landsat-5 bands with products derived from the Landsat imagery (see below). The second method used the HANTS algorithm to calculate adjusted time series images based on NDVI layers derived from Landsat imagery.

In the first method, the reflective Landsat bands were combined with products derived from the four selected Landsat datasets. Different stack combinations included some or all of the following:

- Radiometrically corrected Landsat reflective bands 1 – 5 and 7
- Contrast Texture data calculated for each of the radiometrically corrected Landsat reflective bands using a 3 by 3 pixel window
- Land Surface Temperature (LST) data derived from the Landsat thermal infrared (TIR) band 6
- Tasseled Cap data derived from the Landsat imagery

Although the Tasseled Cap data contain the same spectral information as the reflectance bands, preliminary investigation showed that combining the two types of data often increased classification accuracy. Images from approximately the same time of the year were selected to provide consistency between 2000 – 2001 and 2010 – 2011 trials (Table 1). The ENVI FLAASH MODULE™ (an add-on that can be purchased for the ENVI™ software package) was used to convert the satellite sensor radiance to a surface reflectance for all of the Landsat TM bands except the TIR band. LST can reveal areas with cooler surfaces (e.g., shaded areas) and possibly variations in temperature caused by different rates of evapotranspiration between plant species. Although TIR surface radiance will provide similar information as LST, conversion from surface radiance to LST is simple and LST is easier to understand.

Texture refers to the spatial distribution of tonal variations within an image (e.g., in a Landsat band).[27] This study used the grey level co-occurrence matrix to calculate the contrast texture. Texture information is most useful when a land-cover class has a unique texture: For example,

a stand of trees with uniform canopy height, water features, or an agricultural field;[28] saltcedar

can form dense stands with near uniform height, so texture may be an additional characteristic

that can help with its identification.

The land surface temperature (LST) was derived from the TIR band (band 6) of the Landsat

data using three steps. The first step was to convert the dataset digital numbers to at-sensor

radiance. The second step was to convert the Top of Atmosphere (TOA) radiance to surface

radiance using atmospheric correction factors. The final step was to convert the surface

radiance to LST. In the first step, the digital numbers comprising the Landsat TIR data were

converted to the at-sensor radiance using:[29]

$$L_{\lambda}^{at-sensor} = \left(\frac{LMAX_A - LMIN_A}{Q_{calmax} - Q_{calmin}}\right)(Q_{cal} - Q_{calmin}) + LMIN_A \qquad (1)$$

where $L_{\lambda}^{at-sensor}$ is the at-sensor radiance (W·m^{-2}·sr^{-1}·μm^{-1}), *Qcal* is the quantized calibrated

pixel value, *Qcalmin* is the minimum quantized calibrated pixel value corresponding to *LMIN$_A$*,

Qcalmax is the maximum quantized calibrated pixel value corresponding to *LMAX$_A$*, *LMIN$_A$* is

the spectral at-sensor radiance that is scaled to *Qcalmin* (W·m^{-2}·sr^{-1}·μm^{-1}), and *LMAX$_A$* is the

spectral at-sensor radiance that is scaled to *Qcalmax* (W·m^{-2}·sr^{-1}·μm^{-1}).

For the second step, the NAMCORR atmospheric correction parameter calculator was used to

derive parameters for upwelling radiance, downwelling radiance, and transmissivity. The

NARR data used for the NAMCORR calculations was obtained for the nearest data point

southwest of the study area. Not only was this the closest data point, it is also located in a

riparian area similar to the study area. Once the correction parameters are obtained, they can be

used to convert the TOA radiance to surface radiance. The equation used for converting TOA radiance to surface radiance is:[30]

$$L_\lambda^{TOA} = \tau_\lambda \left[\varepsilon_\lambda L_\lambda + (1 - \varepsilon_\lambda) L_\lambda^{atm\downarrow} \right] + L_\lambda^{atm\uparrow} \tag{2}$$

which can be rearranged as:

$$L_\lambda = \frac{1}{\varepsilon_\lambda} \left[\frac{L_\lambda^{TOA} - L_\lambda^{atm\uparrow}}{\tau_\lambda} - (1 - \varepsilon_\lambda) L_\lambda^{atm\downarrow} \right] \tag{3}$$

where L_λ is the surface radiance (W m^{-2} sr^{-1} μm^{-1}), ε_λ is the emissivity of the surface object (unitless), τ_λ is the atmospheric transmittance (decimal percent), L_λ^{TOA} is the TOA radiance (W m^{-2} sr^{-1} μm^{-1}), $L_\lambda^{atm\uparrow}$ is the upwelling atmospheric radiance (W m^{-2} sr^{-1} μm^{-1}), and $L_\lambda^{atm\downarrow}$ is the downwelling atmospheric radiance (W m^{-2} sr^{-1} μm^{-1}). This equation depends on using the correct value for emissivity. Unfortunately, Landsat-5 data do not provide enough information to derive both ε_λ and LST, so other solutions are required.[31] Some methods assume a relationship between the leaf area index (LAI) and the surface emissivity[32] with assumed emissivity value of 0.98 for areas where the LAI is greater than 3.0. For this investigation, nearly year-round vegetation cover with LAI values greater than 3.0 was assumed for the riparian area; therefore, the corresponding emissivity value of 0.98 was used.

The final step in the conversion process is to convert the surface radiance to LST. The Landsat specific approximation of the Planck function used to convert radiance values to LST is expressed as:

$$T = \frac{k_2}{\ln\left(\frac{k_1}{L_\lambda} + 1\right)} \tag{4}$$

where T is the temperature in Kelvin, k_1 and k_2 are Landsat calibration constants, and L_λ is the spectral radiance.[28, 29]

Initial pre-trials revealed the importance of having accurate training data for the classification process. To select the best training points, four main types of information were used: BOR land-cover classification maps, orthophotos, manually collected field data, and spectral profiles extracted from the Landsat data. The goal was to determine (1) which areas were exclusively saltcedar, and (2) which areas had either no saltcedar or a combination of saltcedar and another land-cover type. One heuristic commonly used to determine the number of training points is to select between 10 and 30 training points per class and map layer used in the classification process.[33] Using a full stack of 64 layers and 2 classes would require a minimum of 1280 training points, which is unrealistic for this study area (64 layers ×10 training points per layer per class × 2 classes = 1280 training points). A study comparing classification results for a binary classification scheme (cotton vs. not cotton) found that using 70 training points gave just as good results as using 450 training points.[34] As a compromise, 100 training points per class were initially selected for a total of 200 training points.

Preliminary classifications revealed that a number of agricultural and rangeland areas adjacent to the study area were misclassified as saltcedar. Although these areas were outside the study area, they were included in the classification process because using a rectangular computational area simplifies the data processing and classification steps. The relevant classification results for the irregularly shaped riparian study area were later extracted from the rectangular area for the final analysis. Additional training data were added to reduce the misclassification of agricultural and rangeland areas in the larger rectangular area, based on the assumption that the classification for the study area would also be improved. Sixty more

training points per class were added for a total of 320 training points (2 classes × (100 training point + 60 additional training points) = 320 training points).

The BOR land-cover classification maps were used to identify areas that could be used to collect field data. The selected sites were visited and the coordinates for areas with various combinations of saltcedar and other vegetation were recorded using a handheld Garmin® 60Cx GPS unit. The GPS data were plotted on the orthophotos and BOR maps using ESRI® ArcMap™. The majority of the training points were selected based on the GPS data because the land-cover type for these areas was known. After learning how different land-cover types appeared in the orthophotos, training data for unvisited areas were added. This method made it possible to include training data for some areas that were inaccessible.

The six reflective Landsat bands for the four seasons in a series were stacked and the spectral profile for each training point was extracted. When the profiles for a point did not match the spectral profiles for the majority of the points in the same class, that point was replaced with a new training point judged to be more representative of the class. This exercise was used to refine all the saltcedar training data. It did not work with the non-saltcedar training data because the spectral profiles for the different land covers were too variable to interpret. Thus, some data representing saltcedar may have inadvertently been included with the non-saltcedar training data.

For the classification methods tested, profiles comprising various combinations of previously described 64 layers were used (Table 2). There is a tendency to assume that the more information that is used, the better the classification results will be. However, sometimes just a few layers are sufficient to provide the desired information[35].

Table 2 Classification combinations and the number of layers

Layers	Classification Layer Combinations							
	A	**B**	**C**	**D**	**E**	**F**	**G**	**H**
Spring Reflective	6	6	6	6	6	6	6	6
Spring Reflective Texture	6		6	6				
Summer Reflective	6	6	6	6	6	6	6	6
Summer Reflective Texture	6		6	6				
Fall Reflective	6	6	6	6	6	6	6	6
Fall Reflective Texture	6		6	6				
Winter Reflective	6	6		6		6		
Winter Reflective Texture	6			6				
Spring LST	1	1	1		1			
Summer LST	1	1	1		1			
Fall LST	1	1	1		1			
Winter LST	1	1						
Spring Tasseled Cap	3	3	3	3	3	3	3	
Summer Tasseled Cap	3	3	3	3	3	3	3	
Fall Tasseled Cap	3	3	3	3	3	3	3	
Winter Tasseled Cap	3	3		3		3		
Total layers	64	40	48	60	30	36	27	18

Combination	Description
A	All layers
B	No Texture
C	No Winter
D	No LST
E	No Texture or Winter
F	No Texture or LST
G	No texture, Winter, or LST
H	Spring, summer, and fall, reflective bands only

All the classifications were performed using ENVI™ software (ENVI™ 4.8). Support Vector Machine (SVM), and Neural Networks (NN) classification methods were used for this study. To minimize the number of choices necessary to perform the SVM classification, the default radial basis function kernel type was used. The default gamma in kernel function (calculated internally by the ENVI™ software based on the number of layers used) and the default penalty parameter of 100 were used. For the NN classification, the default logistic activation method, the training threshold contribution (0.9), and the default training momentum (0.9) settings were used. The training rate was changed from 0.2 to 0.01 and the number of hidden layers from one to three because pre-trials indicated that this combination often produced higher accuracies.

2.4 Classification - HANTS Algorithm

The HANTS algorithm was applied to NDVI data because it has been observed that NDVI can be used to derive the phenological path of plants, and from this, one can determine plant types.[19] NDVI is calculated from Landsat data using:

$$NDVI = \frac{\rho_{NIR} - \rho_{RED}}{\rho_{NIR} + \rho_{RED}} \tag{5}$$

where ρ_{NIR} is the near infrared (NIR) band reflectance value, and ρ_{RED} is the red (RED) band reflectance value. The NDVI values range from negative one to positive one, with the highest positive numbers being associated with dense green vegetation and the lower positive numbers being associated with drier, less dense vegetation. Negative numbers are associated with light colored or reflective surfaces such as snow and bare soil.[34] This study used a series of NDVI images to classify saltcedar.

All the Landsat-5 TM satellite data that did not have obvious cloud cover obscuring the study area from Path 34 Row 36 and Path 33 Row 37 for the relevant time periods were downloaded from the Internet.[36] An interactive data language (IDL) program was written to process the large number of files. The IDL program subsetted the red and near infrared (NIR) Landsat bands (Landsat-5 bands 3 and 4) to a rectangular computational area surrounding the riparian study area. For the HANTS algorithm classification, a simple conversion to TOA reflectance was used prior to calculating NDVI. This makes the method accessible to agencies that may not have the tools for converting satellite sensor radiance to a surface reflectance. Each Landsat band´s digital number (DN) values were converted to sensor radiance using the bias and gain factors for a specific band provided in the Landsat metadata using:[28]

$$L_\lambda \ = \ DN \ * \ gain \ + \ bias \tag{6}$$

where L_λ is the sensor radiance (W m^{-2} sr^{-1} μm^{-1}), and DN is the band's digital number. The bands were then calibrated to TOA reflectance using the earth–sun distance and the sun elevation angle provided in the Landsat metadata using:

$$TOA_{reflectance} \ = \ \frac{\pi * L_\lambda * d^2}{ESUN_\lambda * \sin(sun\ elevation\ angle)} \tag{7}$$

where π is ≈ 3.14159, L_λ is the sensor radiance (W m^{-2} sr^{-1} μm^{-1}), d is the earth–sun distance (astronomical units), and $ESUN_\lambda$ is the mean exoatmospheric solar irradiance (W m^{-2} μm^{-1}). In the final step of the IDL program, the NDVI values were calculated.

The normalized NDVI values from negative one to positive one were re-scaled to values between 0 and 2,000 to facilitate the interpretation of the HANTS results. The resulting NDVI images were manually inspected and images with previously undetected cloud cover or

alignment problems were rejected. The process left 30 NDVI images for the 2000 - 2001 period and 42 NDVI images for the 2010 – 2011 period.

Several time series and parameter combinations were compared for the HANTS algorithm based classifications (Table 3). The starting dates for the one-year series begin with the Landsat scene where the maximum NDVI values are at the lowest part of the annual cycle (Day 0 = 2/2/2000 and Day 0 = 2/13/2010). An extended NDVI series (Fig. 2) that captured the declining NDVI values from the preceding cycle and the rising NDVI values from the following cycle was also tested (11/14/1999 – 4/18/2001; 11/18/2009 – 5/8/2011).

To maintain correspondence with the HANTS software naming conventions, in the following text "pif" refers to the HANTS input NDVI data, "pof" refers to the HANTS output containing the calculated amplitude and phase values, and "psf" refers to the HANTS output containing the calculated smoothed NDVI values. For this investigation, the one-year NDVI series and the extended NDVI series were further subdivided into tests with different numbers of frequencies (i.e., the one-year base frequency and the first harmonics of the base frequency). One set of tests used curves derived by combining the base frequency and the first two harmonics (3 frequencies total) and another set of tests used curves derived by combining the base frequency and the first four harmonics (5 frequencies total). For each set of tests HANTS produced the amplitude and phase (pof) images for each frequency, and based on the selected starting date, ending date, and interval, HANTS produced a smoothed NDVI time series reconstruction (psf). For this study, a reconstructed series of images for 365 days at five-day intervals was selected (365 days / 5 days per interval = 74 reconstructed images).

Table 3 HANTS parameters classification matrix.

Layer Combinations	Year	#layers	FET[a]	Frequency	D[b]	DF[c]	DOD[d]
HANTS 24 pif	2000/2001	24	20	-	-	-	-
HANTS FET20 5F 24 pof	2000/2001	24	20	5	11	6	7
HANTS FET20 5F 24 psf	2000/2001	24	20	5	11	6	7
HANTS FET20 3F 24 pof	2000/2001	24	20	3	7	6	11
HANTS FET20 3F 24 psf	2000/2001	24	20	3	7	6	11
HANTS 30 pif	2000/2001	30	20	-	-	-	-
HANTS FET20 5F 30 pof	2000/2001	30	20	5	11	6	13
HANTS FET20 5F 30 psf	2000/2001	30	20	5	11	6	13
HANTS FET20 3F 30 pof	2000/2001	30	20	3	7	6	17
HANTS FET20 3F 30 psf	2000/2001	30	20	3	7	6	17
HANTS 30 pif	2010/2011	30	20	-	-	-	-
HANTS FET20 5F 30 pof	2010/2011	30	20	5	11	6	13
HANTS FET20 5F 30 psf	2010/2011	30	20	5	11	6	13
HANTS FET20 3F 30 pof	2010/2011	30	20	3	7	6	17
HANTS FET20 3F 30 psf	2010/2011	30	20	3	7	6	17
HANTS 42 pif	2010/2011	42	20	-	-	-	-
HANTS FET20 5F 42 pof	2010/2011	42	20	5	11	6	25
HANTS FET20 5F 42 psf	2010/2011	42	20	5	11	6	25
HANTS FET20 3F 42 pof	2010/2011	42	20	3	7	6	29
HANTS FET20 3F 42 psf	2010/2011	42	20	3	7	6	29

[a] Fit Error Tolerance (FET) is the absolute deviation allowable in curve fitting

[b] D equals two times the number of frequencies plus one

[c] Degrees of Freedom (DF) equals #layers – (D + DOD), maximum number of samples that can be eliminated in curve fitting

[d] Degrees of Over Determinedness (DOD)

For each period (2000 – 2001 and 2010 – 2011), the SVM and NN classifiers were used. The classifications were run on the stacked NDVI images as a control (i.e., pif layer combinations). The classifications were repeated using both the stacked amplitude and phase images (i.e., pof layer combinations), and the smoothed time series (i.e., psf layer combinations). In summary, two different frequencies combinations (3 and 5) and two different series (a one-year cycle; and an extended cycle) were run.
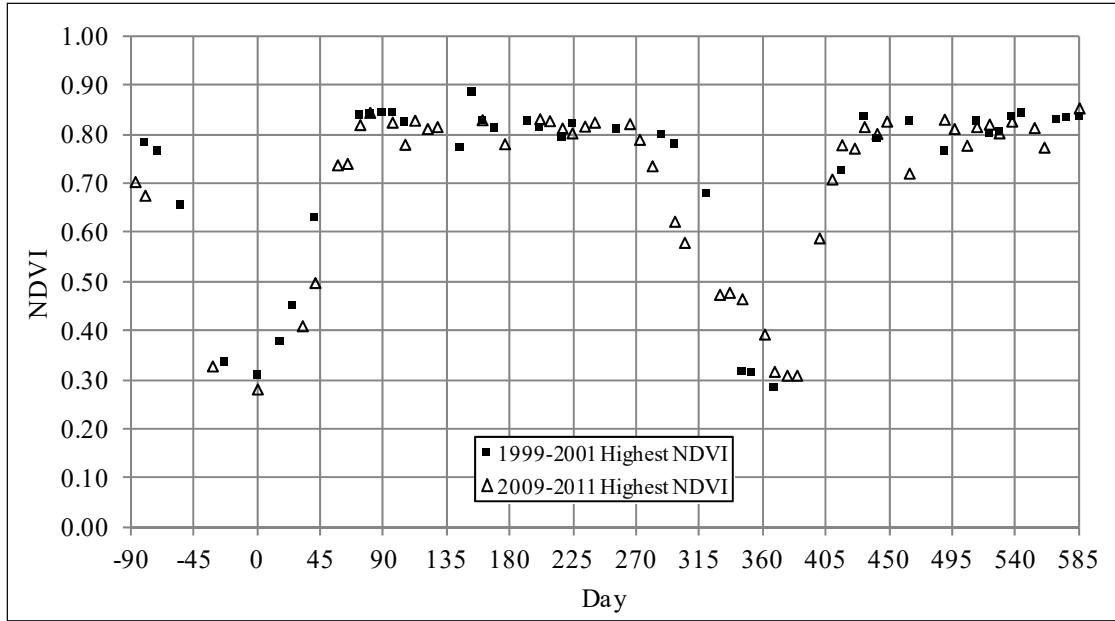
Fig. 2 Highest NDVI value per Landsat scene. One-year NDVI cycle begins Day 0. The extended NDVI series includes falling (Day < 0) NDVI values from the preceding cycle and rising (Day > 365) NDVI values from the following cycle; data series for years 1999 –2001 and 2009 – 2011.

2.5 Accuracy Assessment

The binomial distribution was used to determine how many data points were needed for the accuracy assessment. This distribution is valid for use with land-cover classification maps that only have two classes.[37, 38] The number of points is calculated using:

$$N = \frac{Z^2 pq}{E^2} \tag{8}$$

where N is the number of reference points required, Z is the standard score based on the selected confidence interval, p is the expected accuracy, $q = 1 - p$, and E is the allowable error. The expected overall accuracy p was set to 85%, which was considered the lowest

acceptable accuracy for this study. For this level of accuracy, the accuracies were expected to vary by at least 5%, so this was used as the allowable error. Using a 95 percent two-sided confidence probability, the binomial distribution indicated that 204 reference points were needed for the accuracy assessment. This was rounded down to 200 points to make it easier to compare the results of the various accuracy assessments.

A statistically valid method for selecting the reference points was also needed. The best method would be to select 200 points randomly; however, the saltcedar stands might not be adequately represented using this method. To ensure that saltcedar was included, the stratified random method was used and 100 points were randomly selected to represent the saltcedar class, and 100 points were randomly selected to represent the non-saltcedar class. The best initial information concerning the location of saltcedar stands was the BOR landcover maps. The BOR maps and ArcGIS™ were used to locate areas that were classified as saltcedar only. Only areas classified as saltcedar in both the 2002 and 2008 BOR landcover maps were used to increase the likelihood that there were areas with only saltcedar among the randomly selected points.

A tool in ArcGIS™ was used to assign randomly 100 points to the areas designated as saltcedar only, and to randomly assign the remaining 100 points to the other areas. The other areas could be any land-cover type, ranging from areas with no saltcedar to area with saltcedar mixed in with some other land-cover type. It was necessary to check each reference point manually to verify the point was in the correct class. Each point was visually compared to its location in the orthophotos and the point's spectral profile was compared to the saltcedar profiles previously generated from the training data. If these comparisons did not match, the point was transferred to the correct class.

When the re-classification of the reference points was complete, the number of saltcedar reference points was less than 50% of the total number of reference points for both classification periods. Since the location of the saltcedar stands could vary from one classification period to the next, the verification process was performed for both classification periods. The same 200 points were re-used for each period to maintain some consistency between classifications; however, the ratio of saltcedar reference points to non-saltcedar points varied between classification periods.

3   Results and Discussion

At Bosque del Apache NWR, the overall saltcedar prediction accuracies from 2000 – 2001 for the stacked data ranged from 88.0 to 91.0% (Table 4). The corresponding overall accuracies obtained using the HANTS algorithm ranged from 81.5 to 90.5%. The lowest accuracy for the stacked data was 71.19% for the producer's accuracy and 50.85% for the HANTS algorithm producer's accuracy.

The 2000 – 2001 stacked data classification with the highest accuracy used the spring, summer, and fall reflective, LST, and Tasseled Cap layers (Combination E, Table 2) with the SVM classification method (Fig. 3(a)). The saltcedar producer's accuracy was 81.36%, and the user's accuracy was 87.27%. The producer's accuracy for areas other than saltcedar was 95.04% and the user's accuracy was 92.41%. The overall accuracy was 91.0%. The corresponding HANTS classification with the highest saltcedar producer's accuracy used 5 frequencies and a smoothed time series (psf) based on the extended NDVI series (30 NDVI datasets) with the NN classification method (Fig. 3(b)). The saltcedar producer's accuracy was

79.66%, and the user's accuracy was 81.03%. The producer's accuracy for areas other than saltcedar was 92.20% and the user's accuracy was 91.55%. The overall accuracy was 88.5%.

The overall accuracies from 2010 – 2011 for the stacked data ranged from 88.0 to 89.0% (Table 5). The corresponding overall accuracies obtained using the HANTS algorithm ranged from 77.5 to 85.0%. The lowest accuracy for the stacked data was 72.84% for the producer's accuracy and 45.68% for the HANTS algorithm producer's accuracy.

The 2010 – 2011 stacked data classification with the highest accuracy used the spring, summer, and fall reflective, LST, and Tasseled Cap layers (Combination E, Table 2) with the SVM classification method (Fig. 3(c)). The saltcedar producer's accuracy was 83.95%, and the user's accuracy was 88.31%. The producer's accuracy for areas other than saltcedar was 92.44% and the user's accuracy was 89.43%. The overall accuracy was 89.0%. The corresponding HANTS classification used 5 frequencies and the stacked amplitude and phase images (pof) based on the extended NDVI series (42 NDVI datasets) with the NN classification method (Fig. 3(d)). The saltcedar producer's accuracy was 81.48%, and the user's accuracy was 81.48%. The producer's accuracy for areas other than saltcedar was 87.39% and the user's accuracy was 87.39%. The overall accuracy was 85.0%.

The results indicate that not all the stacked layers were necessary. Including the texture layers and winter layers actually reduced the accuracy. The fact that the most accurate stacked data classifications for both 2000 – 2001 and 2010 - 2011 used the same layers and classification algorithm is a coincidence. A previous investigation at the same study area using four time series found that the layer combination and classification algorithm with the best accuracy varied over time.[39] In one case, a simple stack of the reflective bands gave the best accuracy

and in most cases the NN algorithm produced higher accuracies than the SVM algorithm. However, this study is focused on comparing the stacked method with the HANTS algorithm method.

In both cases, the combination of parameters and classification algorithms that produced the highest accuracy was found through trial and error. This investigation revealed that the range of accuracies varied more for the HANTS trials. It also demonstrated that the extended NDVI series produced better accuracies than the one-year cycle. If a study is to be repeated for a given area, a sensitivity analysis to determine which parameters affect the accuracies most could be performed. The entire classification process could also be automated to test a larger number of parameter combinations, which could result in higher accuracies. However high the accuracies are, the results must reflect reality and not just a set of reference data.

	saltcedar				Other				Overall Accuracy	
	Producer's Accuracy		User's Accuracy		Producer's Accuracy		User's Accuracy			
Layer Combinations	SVM	NN	SVM	NN	SVM	NN	SVM	NN	SVM	NN
All layers + NDVI	71.19	81.36	89.36	84.21	96.45	93.62	88.89	92.31	89.0	90.0
All layers	69.49	74.58	87.23	89.80	95.74	96.45	88.24	90.07	88.0	90.0
No Texture	67.80	74.58	88.89	86.27	96.45	95.04	87.74	89.93	88.0	89.0
No Winter	72.88	79.66	84.31	81.03	94.33	92.20	89.26	91.55	88.0	88.5
No Temperature	88.14	79.66	76.47	83.93	88.65	93.62	94.70	91.67	88.5	89.5
No Texture or Winter	81.36	79.66	87.27	88.68	95.04	95.74	92.41	91.84	91.0	91.0
No Texture or Temperature	84.75	77.97	83.33	83.64	92.91	93.62	93.57	91.03	90.5	89.0
No Texture, Winter, or Temperature	83.05	79.66	80.33	88.68	91.49	95.74	92.81	91.84	89.0	91.0
3 Seasons, Landsat bands only	84.75	79.66	80.65	88.68	91.49	95.74	93.48	91.84	89.5	91.0
	SVM	NN	SVM	NN	SVM	NN	SVM	NN	SVM	NN
HANTS 30 pif	69.49	71.19	89.13	95.45	96.45	98.58	88.31	89.10	88.5	90.5
HANTS FET20 5F 30 pof	72.88	74.58	86.00	89.80	95.04	96.45	89.33	90.07	88.5	90.0
HANTS FET20 5F 30 psf	50.85	79.66	85.71	81.03	96.45	92.20	82.42	91.55	83.0	88.5
HANTS FET20 3F 30 pof	50.85	71.19	78.95	77.78	94.33	91.49	82.10	88.36	81.5	85.5
HANTS FET20 3F 30 psf	52.54	74.58	86.11	81.48	96.45	92.91	82.93	89.73	83.5	87.5
HANTS 24 pif	69.49	71.19	93.18	89.36	97.87	96.45	88.46	88.89	89.5	89.0
HANTS FET20 5F 24 pof	61.02	69.49	73.47	89.13	90.78	96.45	84.77	88.31	82.0	88.5
HANTS FET20 5F 24 psf	45.76	67.80	87.10	86.96	97.16	95.74	81.07	87.96	82.0	87.5
HANTS FET20 3F 24 pof	64.41	71.19	82.61	80.77	94.33	92.91	86.36	88.51	85.5	86.5
HANTS FET20 3F 24 psf	50.85	71.19	78.95	77.78	94.33	91.49	82.10	88.36	81.5	85.5

	saltcedar				Not saltcedar					
	Producer's Accuracy		User's Accuracy		Producer's Accuracy		User's Accuracy		Overall Accuracy	
Layer Combinations	SVM	NN	SVM	NN	SVM	NN	SVM	NN	SVM	NN
All layers + NDVI	79.01	87.65	88.89	74.74	93.28	79.83	86.72	90.48	87.5	83.0
All layers	81.48	82.72	86.84	76.14	91.60	82.35	87.90	87.50	87.5	82.5
No Texture	82.72	91.36	85.90	75.51	90.76	79.83	88.52	93.14	87.5	84.5
No Winter	76.54	74.07	87.32	80.00	92.44	87.39	85.27	83.20	86.0	82.0
No Temperature	76.54	87.65	88.57	74.74	93.28	79.83	85.38	90.48	86.5	83.0
No Texture or Winter	83.95	82.72	88.31	75.28	92.44	81.51	89.43	87.39	89.0	82.0
No Texture or Temperature	85.19	88.89	83.13	77.42	88.24	82.35	89.74	91.59	87.0	85.0
No Temperature or Winter	74.07	79.01	88.24	73.56	93.28	80.67	84.09	84.96	85.5	80.0
No Texture, Winter, or Temperature	82.72	72.84	84.81	83.10	89.92	89.92	88.43	82.95	87.0	83.0
3 Seasons, Landsat bands only	82.72	76.54	83.75	77.50	89.08	84.87	88.33	84.17	86.5	81.5
	SVM	NN	SVM	NN	SVM	NN	SVM	NN	SVM	NN
HANTS 42 pif	64.20	45.68	83.87	94.87	91.60	98.32	78.99	72.67	80.5	77.0
HANTS FET20 5F 42 pof	76.54	81.48	75.61	81.48	83.19	87.39	83.90	87.39	80.5	85.0
HANTS FET20 5F 42 psf	67.90	80.25	82.09	74.71	89.92	81.51	80.45	85.84	81.0	81.0
HANTS FET20 3F 42 pof	80.25	93.83	71.43	67.26	78.15	68.91	85.32	94.25	79.0	79.0
HANTS FET20 3F 42 psf	67.90	46.91	78.57	76.00	87.39	89.92	80.00	71.33	79.5	72.5
HANTS 30 pif	62.96	51.85	82.26	95.45	90.76	98.32	78.26	75.00	79.5	79.5
HANTS FET20 5F 30 pof	72.84	90.12	72.84	69.52	81.51	73.11	81.51	91.58	78.0	80.0
HANTS FET20 5F 30 psf	64.20	54.32	76.47	80.00	86.55	90.76	78.03	74.48	77.5	76.0
HANTS FET20 3F 30 pof	66.67	79.01	78.26	73.56	87.39	80.67	79.39	84.96	79.0	80.0
HANTS FET20 3F 30 psf	62.96	92.59	80.95	71.12	89.92	75.63	78.10	93.75	79.0	82.5
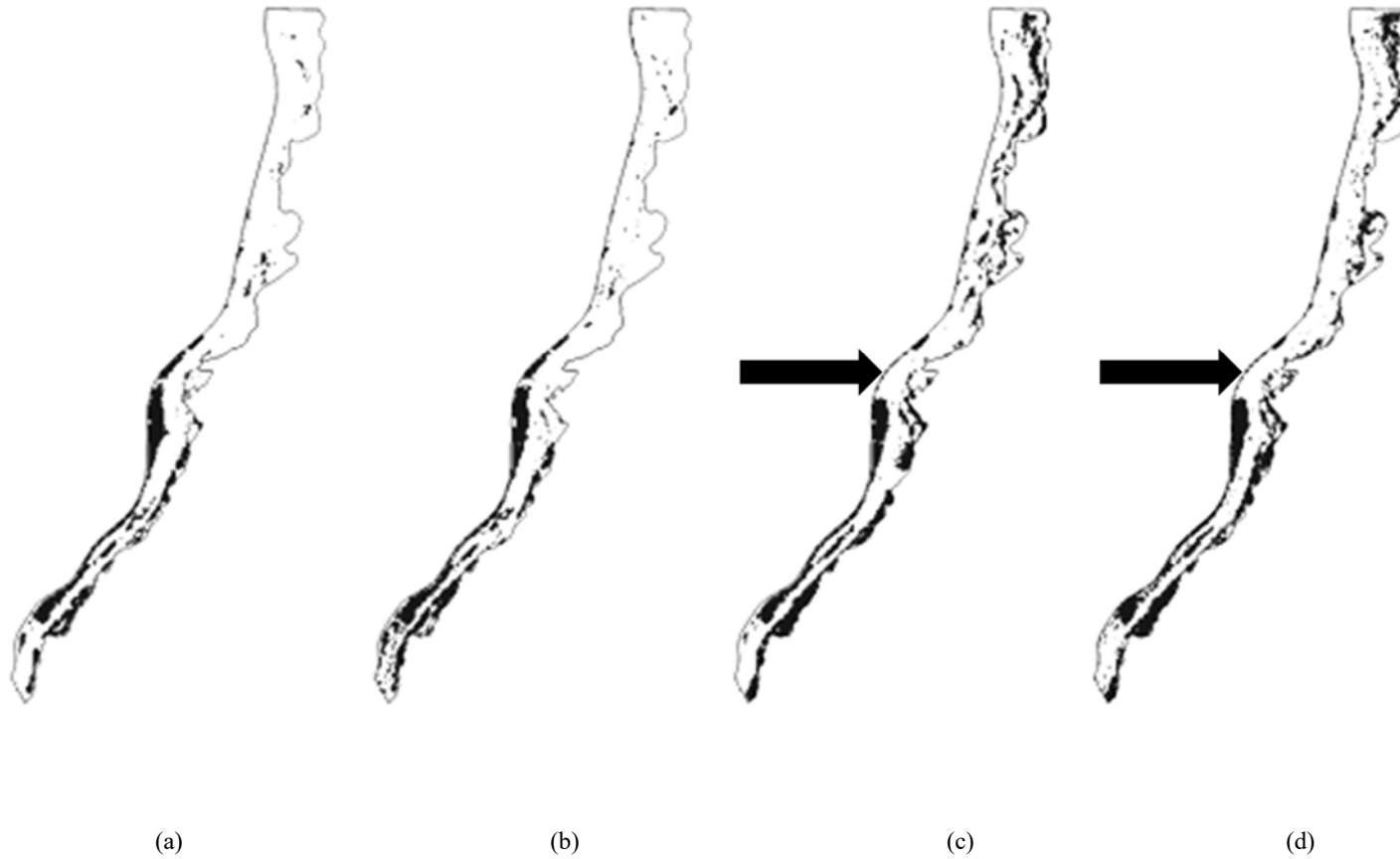
Fig. 3 Riparian area saltcedar classification results with the highest accuracies: (a) 2000-2001 Stacked, (b) 2000-2001 HANTS, (c) 2010-2011 Stacked, (d) 2010-2011 HANTS. Areas classified as saltcedar are shown in black. Arrows indicate areas where saltcedar eradication measures were implemented.

Comparing the mapped classification results for the stacked data and the mapped classification results for the HANTS algorithm with the highest accuracies shows that the two methods can produce similar results (Fig. 3). Both the stacked data and HANTS algorithm methods show that in 2000 – 2001 saltcedar already dominated large areas in the southern half of the riparian area. Both methods also show the results of saltcedar eradication efforts (arrows in Fig. 3(c) and Fig. 3(d)) and the expansion of the saltcedar in the northern half of the riparian area between 2000 and 2010. The agreement between the two methods is best where saltcedar forms dense, continuous, and homogenous stands. There is more variation in the classification results where saltcedar borders areas with other vegetation types or where there are mixed pixels (i.e., where saltcedar is spreading to areas with other types of vegetation). The results indicate that both methods provide useful information for land managers.

The tabulated accuracy results (Tables 4 and 5) reveal that the accuracy of a particular method and dataset can vary from year to year. This is partly because the areas being classified often have similar characteristics. For example, areas dominated by saltcedar have similar NDVI values as the areas dominated by cottonwood. In some years, the area with the highest NDVI values can change from saltcedar to cottonwood over the course of the season as revealed by the output of the HANTS algorithm smoothed reconstruction (Fig. 4). This demonstrates the utility of using a variety of data sets and classification algorithms if the time and resources are available. This is especially important in riparian areas where the channels may change course over time and where drought and flood events can produce erratic changes over the course of a year.
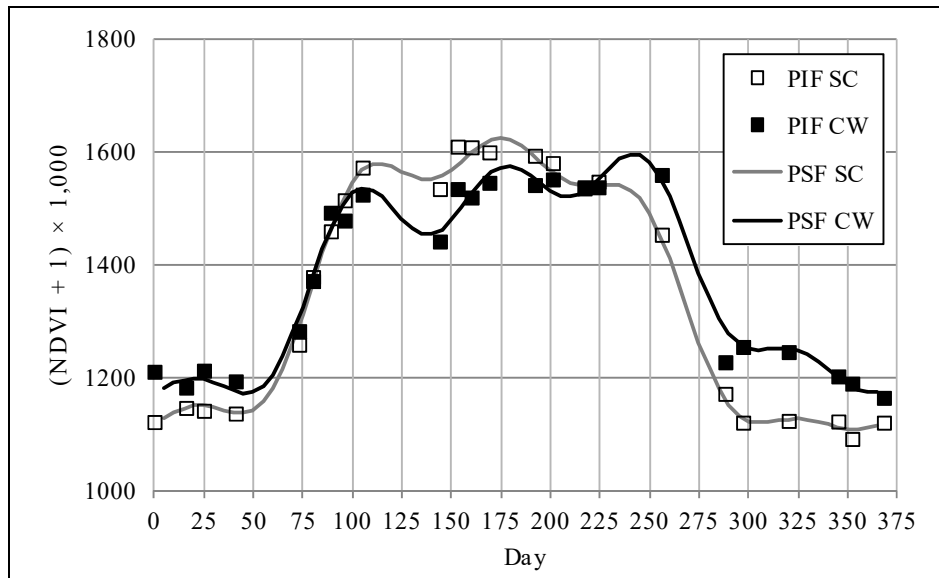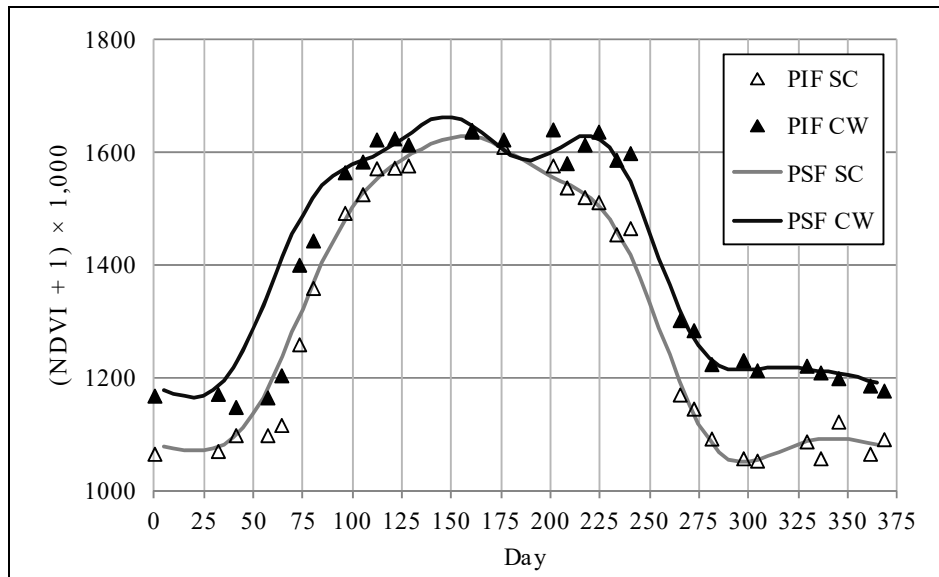
Fig. 4 Example of NDVI data points (PIF) and smoothed time series lines (PSF) using the HANTS algorithm for saltcedar (SC) and cottonwood (CW) dominated areas.

For both the HANTS based classification and the stacked layer classification, a number of

trials were necessary to determine which combination of parameters or layers provide the

highest accuracies. While the stacked layers provided somewhat higher classification

accuracies, the preparation of the layers is time consuming and may be beyond the skill level of some researchers. It also used atmospheric correction tools that may not be available to the researcher. The advantage of using the HANTS algorithm is that calculating the smoothed reconstruction is relatively rapid and easy to understand. The direct classification of the amplitude and phase data used to produce the smoothed reconstruction provides an additional path for classification with relatively little extra effort. What is interesting is that the HANTS algorithm-based classification method can use phenological information embedded in the data even when a researcher has no prior knowledge of the classified plant's phenology. The smoothed reconstruction may even reveal important phenological information that is useful in itself. The disadvantage is that a large number of remote sensing datasets are required to obtain useful classification results as compared to the traditional method that only used four data sets per classification; however, there may be ways to overcome this disadvantage.

Other satellite sensors exist with spectral and spatial resolution similar enough to the Landsat red and NIR bands that could be used to augment the Landsat data and data from new satellite sensors should be available in the near future. Using multiple satellite sensors is possible because the HANTS algorithm does not require the data to be spaced evenly over time. Also, this study specifically used cloud-free imagery even though this is not necessary. One significant advantage of the HANTS algorithm is that it can utilize imagery with some cloud cover. The HANTS algorithm parameters can be adjusted to remove the cloud contamination and the resulting smoothed reconstruction (and/or amplitude and phase data) can be used to perform the classification.

Another advantage is that calculating NDVI is simple and the HANTS algorithm computations are relatively rapid such that the method can be performed using any computer hardware and software combination capable of manipulating and classifying satellite imagery. A researcher with programming skills could automate the entire process and

perform a large number of trials using different parameters to discover the combinations with the best accuracies. Future classification work using the HANTS algorithm could investigate other vegetation indices or any other data characteristic(s) (e.g., albedo, land surface temperature) that vary over space and time.

4   Conclusion

Remote sensing tools based on Landsat data can provide land managers with useful information about saltcedar expansion in riparian areas of the desert Southwest. Normally inaccessible areas can be evaluated without disturbing vulnerable wildlife or vegetation. This research shows traditional classification methods can be complemented or replaced entirely using the HANTS algorithm. The phenological changes revealed by the smoothed HANTS reconstruction of NDVI data can be used directly to classify areas with saltcedar, or the reconstruction can be used to aid the selection of data used with other classification methods. The HANTS algorithm software could also be incorporated in an automated classification processes to test a wide variety of frequencies and parameters, thus identifying combinations with the highest accuracies. The HANTS algorithm and the method described in this research provides a low cost (or no cost depending on the software selected) alternative to methods requiring more expensive software, and should be investigated by agencies with limited resources that need to perform similar classification and mapping tasks.

5   References

1. J.L. Moore, J.P. King, A.S. Bawazir, and T.W. Sammis, *A bibliography of evapotranspiration with special emphasis on riparian vegetation* (WRRI Miscellaneous Report No. M28), Water Resources Research Institute, Las Cruces, NM (2004).
2. Y. Hamada, D.A. Stow, L.L. Coulter, J.C. Jafolla, and L.W. Hendricks, "Detecting Tamarisk species (*Tamarix* spp.) in riparian habitats of Southern California using high

spatial resolution hyperspectral imagery," *Remote Sensing of Environment*, **109**(2), 237–248 (2007) [doi:10.1016/j.rse.2007.01.003].

3. O.Z. Akasheh, C.M. Neale, and H. Jayanthi, "Detailed mapping of riparian vegetation in the middle Rio Grande River using high resolution multi-spectral airborne remote sensing," *Journal of Arid Environments*, 72(9), 1734-1744 (2008) [doi:10.1016/j.jaridenv.2008.03.014].

4. R. Pu, P. Gong, Y. Tian, X. Miao, R.I. Carruthers, and G.L. Anderson, "Using classification and NDVI differencing methods for monitoring sparse vegetation coverage: a case study of saltcedar in Nevada, USA," *International Journal of Remote Sensing,* **29**(14), 3987–4011 (2008) [doi:10.1080/01431160801908095].

5. S. Narumalani, D.R. Mishra, R. Wilson, P. Recce, and A. Köhler, "Detecting and mapping four invasive species along the floodplain of North Platte River , Nebraska," *Weed Technology*, **23**(1), 99–107 (2009) [doi:http://dx.doi.org/10.1614/WT-08-007.1].

6. X. Miao, R. Patil, J.S. Heaton, and R.C. Tracy, "Detection and classification of invasive saltcedar through high spatial resolution airborne hyperspectral imagery," *International Journal of Remote Sensing*, **32**(8), 2131–2150 (2011) [doi:10.1080/01431161003674618].

7. J. Morisette, C. Jarnevich, and A. Ullah, "A tamarisk habitat suitability map for the continental United States," *Frontiers in Ecology and the Environment*, **4**(1), 11-17 (2006) [http://dx.doi.org/10.1890/1540-9295(2006)004[0012:ATHSMF]2.0.CO;2].

8. D.P. Groeneveld, and R.P. Watson, "Near-infrared discrimination of leafless saltcedar in wintertime Landsat TM," *International Journal of Remote Sensing*, **29**(12), 3577–3588 (2008) [doi:10.1080/01431160701711078].

9. A.S. Bawazir, Z. Samani, M. Bleiweiss, R. Skaggs, and T. Schmugge, "Using ASTER satellite data to calculate riparian evapotranspiration in the Middle Rio Grande, New Mexico," *International Journal of Remote Sensing*, **30**(21), 5593–5603 (2009) [doi:10.1080/01431160802695683].

10. J.L. Silván-Cárdenas, and L. Wang, "Retrieval of subpixel Tamarix canopy cover from Landsat data along the Forgotten River using linear and nonlinear spectral mixture models," *Remote Sensing of Environment,* **114**(8), 1777–1790 (2010) [doi:10.1016/j.rse.2010.04.003].

11. K.L. Hestir, *Land cover classification and change detection in drylands: An evaluation of remote sensing approaches* (Master's thesis), New Mexico State University, Las Cruces, New Mexico (2012).

12. E.P. Crist, and R.J. Kauth, "The tasseled cap de-mystified," *Photogrammetric Engineering & Remote Sensing,* **52**(1), 81-86 (1986).

13. M. Menenti, S. Azzali, W. Verhoef, and R. van Swol, "Mapping agroecological zones and time lag in vegetation growth by means of Fourier analysis of time series of NDVI images," *Advanced Space Research* **13**(5), 233-237 (1993) [doi:10.1016/0273-1177(93)90550-U].

14. S. Azzali, and M. Menenti, "Mapping vegetation-soil-climate complexes in southern Africa using temporal Fourier analysis of NOAA-AVHRR NDVI data," *International Journal of Remote Sensing,* **21**(5), 973-996 (2000) [doi:10.1080/014311600210380].

15. A. Moody, and D.M. Johnson, "Land-surface phonologies from AVHRR using the discrete Fourier transform," *Remote Sensing of Environment* **75**(2001), 305-323 (2001) [doi:10.1016/S0034-4257(00)00175-9].

16. M.E. Jakubauskas, D.R. Legates, and J.H. Kastens, "Harmonic analysis of time-series AVHRR NDVI data," *Photogrammetric Engineering & Remote Sensing,* **67**(4), 461-470 (2001).

17. M.M. González Loyarte, and M. Menenti, "Impact of rainfall anomalies on Fourier parameters of NDVI time series of northwestern Argentina," *International Journal of Remote Sensing,* **29**(4), 1125-1152 (2008) [doi:10.1080/01431160701355223].

18. G.J. Roerink, M. Menenti, and W. Verhoef, "Reconstructing cloudfree NDVI composites using Fourier analysis of time series," *International Journal of Remote Sensing,* **21**(9), 1911-1917 (2000) [doi:10.1080/014311600209814].

19. L. Jia, H. Shang, G. Hu, and M. Menenti, "Phenological response of vegetation to upstream river flow in the Heihe Rive basin by time series analysis of MODIS data," Hydrology and Earth System Sciences, 15(2011), 1047-1064 (2011) [doi:10.5194/hess-15-1047-2011].

20. A. de Wit, and B. Su, "Deriving Phenological Indicators From Spot-Vgt Data Using The Hants Algorithm," Proc. International SPOT 4/5 - VEGETATION users Conference, (www.vgt.vito.be/vgtapen/pages/fullpapers/Dewit_full.pdf) (2004).

21. Y. Julien, J.A. Sobrinoa, and W. Verhoef, "Changes in land surface temperatures and NDVI values over Europe between 1982 and 1999," *Remote Sensing of Environment*, 103(1), 43-55 (2006) [doi:10.1016/j.rse.2006.03.011].

22. J.P. Taylor, and K.C. McDaniel, "Restoration of saltcedar (*Tamarix sp.*)- infested floodplains on the Bosque del Apache National Wildlife Refuge," *Weed Technology*, **12**(2), 345-352 (1998).

23. A.S. Bawazir, *Saltcedar and Cottonwood riparian evapotranspiration in the Middle Rio Grande*. (Ph.D. Dissertation), New Mexico State University, Las Cruces, New Mexico (2000).

24. NOAA. (2012). NCEP North American Regional Reanalysis (NARR). *U.S. Department of Commerce: National Oceanic & Atmospheric Administration Research*. Retrieved March 13, 2013, from http://www.esrl.noaa.gov/psd/data/gridded/data.narr.html

25. D.C. McCarville, M. Buenemann, M. Bleiweiss, and J. Barsi, "Atmospheric correction of Landsat thermal infrared imagery: A calculator based on North American Regional Reanalysis (NARR) data," *Proc. ASPRS 2011 Annual Conference. Milwaukee, Wisconsin: American Society for Photogrammetry & Remote Sensing* (2011).

26. F. Mesinger, G. DiMego, E. Kalnay, K. Mitchell, P.C. Shafran, W. Ebisuzaki, D. Jović, J. Woollen, E. Rogers, E.H. Berbery, M.B. Ek, Y. Fan, R. Grumbine, W.H. Higgins, Y. Li, G. Manikin, D. Parrish, and W. Shi, "North American Regional Reanalysis," *Bulletin of the American Meteorological Society*, **87**(3), 343–360 (2006) [doi:10.1175/BAMS-87-3-343].

27. R.M. Haralick, K. Shanmugam, and I. Dinstein, "Textural features for image classification," *IEEE Transactions on Systems, Man and Cybernetics*, **SMC-3**(6), 610–621 (1973).

28. J. Gao, *Digital analysis of remotely sensed imagery*, McGraw-Hill, New York (2009).

29. G. Chander, B.L. Markham, and D.L. Helder, "Summary of current radiometric calibration coefficients for Landsat MSS, TM, ETM+, and EO-1 ALI sensors," *Remote Sensing of Environment,* **113**(5): 893-903 (2009) [doi:10.1016/j.rse.2009.01.007].

30. J.A. Barsi, J.R. Schott, F.D. Palluconi, and S.J. Hook, "Validation of a web-based atmospheric correction tool for single thermal band instruments," *Proc. SPIE* **5882,** 58820E-1-58820E-7 (2005) [doi: 10.1117/12.619990].

31. Z. Qin, A. Karnieli, and P. Berliner, "A mono-window algorithm for retrieving land surface temperature from Landsat TM data and its application to the Israel-Egypt

border region," *International Journal of Remote Sensing*, **22**(18), 3719–3746 (2001) [doi:10.1080/01431160010006971].

32. M. Tasumi, Progress in operational estimation of regional evapotranspiration using satellite data (PhD dissertation), University of Idaho. Moscow, Idaho (2003).

33. T.G. Van Niel, T.R. McVicar, and B. Datt, "On the relationship between training sample size and data dimensionality: Monte Carlo analysis of broadband multi-temporal classification," *Remote Sensing of Environment*, 98(4), 468–480 (2005) [doi:10.1016/j.rse.2005.08.011].

34. G.M. Foody, A. Mathur, C. Sanchez-Hernandez, and D.S. Boyd, "Training set size requirements for the classification of a specific class," *Remote Sensing of Environment*, **104**(1), 1–14 (2006) [doi:10.1016/j.rse.2006.03.004].

35. J. R. Jensen, *Introductory digital image processing: A remote sensing perspective,* Pearson Prentice Hall, Upper Saddle River, NJ (2005).

36. U.S. Geological Survey. Global Visualization Viewer. (2014). U.S. Department of the Interior, U.S. Geological Survey. Retrieved March 4, 2014, from http://glovis.usgs.gov/

37. R.G. Congalton, and K. Green, *Assessing the accuracy of remotely sensed data: Principles and practices,* 2nd ed., Taylor & Francis Group, LLC, Boca Raton, FL (2009).

38. K. Fitzpatrick-Lins, "Comparison of sampling procedures and data analysis for a land-use and land-cover map," *Photogrammetric Engineering and Remote Sensing*, **47**(3), 343–351 (1981).

39. D.C. McCarville, *Remote sensing methods for use in the adaptive management of saltcedar* (Tamarix spp.) *at the Bosque del Apache National Wildlife Refuge* (Master's thesis), New Mexico State University, Las Cruces, New Mexico (2013).